Harsh-Environment-Resistant OH-Vibrations-Sensitive Mid-Infrared Water-Ice Photonic Sensor

Javier Martínez, Airán Ródenas, Andreas Stake, Miquel Traveria, Magdalena Aguiló, Javier Solis, Roberto Osellame, Taro Tanaka, Benoit Berton, Shigueo Kimura, Nadine Rehfeld, and Francesc Díaz*

State-of-the-art ultrahigh-sensitivity photonic sensing schemes rely on exposing the evanescent field of tightly confined light to the environment. Yet, this renders an inherent fragility to the device, and since adding a protective layer disables light exposure, there exists a technology gap for highly sensitive harsh-environment-resistant surface photonic sensors. Here, a novel type of mid-infrared waveguide sensors is reported which exploit vibrational resonance-driven directional coupling effects besides absorption, with optical sensing elements that can be buried (≈1–10 μm) and resist systematic exposure to industrial environments without failure. A harsh-environment-resistant, fiber-coupled, surface sensor for monitoring the structural phase of water (liquid-supercooled-solid), as well as the type of ice microstructure (clear rime), is shown. It is demonstrated how this type of sensor can be designed to detect ice layers with nanometric (≈100 nm) to microscopic (≈30 μm or higher) thicknesses, and the first experimental tests both in optical laboratory and in icing wind tunnel inflight aircraft simulation tests are reported.

1. Introduction

Whereas water is the most common liquid on earth, its plethora of anomalous and counterintuitive properties still puzzles scientists and engineers from a wide diversity of fields.[1] Possibly the most abundant state of water in the universe is its solid glass form present in interstellar dust and comets (polyamorphous ice),[1] while on Earth it appears in liquid form, its crystalline hexagonal phase, or in its cubic phase below –80 °C.[2] Yet, there also exists a metastable state of liquid water within the crystalline domain between 0 and –32 °C in which its thermodynamical anomalies manifest most strongly; supercooled water (SCW)[3] is of importance for cell research and the understanding of life at its lower temperature limit, the food and pharmaceutical industries, environmental and climate research sciences, and the aviation industry, among others.

Natural SCW is largely present in cold clouds and it is a recognized hazard for commercial aviation, ultimately hampering achievement of the zero operational accidents international safety goal.[4] When micrometer SCW cloud droplets impinge on a wing surface they immediately freeze, promoting a fast-growing ice accretion layer which can degrade wing performance within seconds with potential loss of control and aircraft stall,[5] a process commonly known as in-flight icing. As modern aircraft design evolves toward adopting advanced wing concepts such as the blended-wing body and low-drag end surfaces for greener and fuel efficient aircrafts, in-flight icing phenomena not only poses a challenge to coming safety regulations but also to the development of next-generation aircrafts. Among the priorities in aeronautics icing research, besides the development of icephobic anti-icing and de-icing coatings,[5,6] is the development of highly reliable ice sensors that can be embedded and distributed across wing surfaces for the automatic control

J. Martínez, Dr. A. Ródenas, Prof. M. Aguiló, Prof. F. Díaz
Departament de Química Física i Inorgànica
Universitat Rovira i Virgili
Campus Sescelades, Marcel•lí Domingo 1, 43007 Tarragona, Spain
E-mail: arodenas@gmail.com

Dr. A. Ródenas, Dr. R. Osellame
Istituto di Fotonica e Nanotecnologie (IFN)
Consiglio Nazionale delle Ricerche (CNR)
Piazza Leonardo da Vinci 32, 20133 Milano, Italy

A. Stake, N. Rehfeld
Fraunhofer-Institut fur Fertigungstechnik und Angewandte Materialforschung (Fraunhofer IFAM)
Wiener Straße 12, 28359 Bremen, Germany

Dr. M. Traveria
Centro de Estudios Superiores de la Aviación (CESDA)
Carretera de l'Aeroport, s/n, 43206 Reus, Spain

Dr. J. Solis
Laser Processing Group
Instituto de Óptica
CSIC, Serrano 121, 28006 Madrid, Spain

T. Tanaka
Fuji Heavy Industries Ltd.
Subaru Corporation
Ebisu Subaru Bldg. 1-20-8, Ebisu, Shibuya-ku, 150-8554 Tokyo, Japan

Dr. B. Berton
Dassault Aviation
78 Quai Marcel Dassault, 92210 Saint-Cloud Cedex, France

Prof. S. Kimura
Faculty of Mechanical Engineering
Kanagawa Institute of Technology
Shimo-Ogino Atsugi Kanagawa, 243-0292 Kanawaga, Japan

The ORCID identification number(s) for the author(s) of this article can be found under https://doi.org/10.1002/admt.201700085.

DOI: 10.1002/admt.201700085

of electrothermal de-icing systems. Current aircraft ice sensors are large, heavy, airflow intrusive, are installed in the aircraft fuselage rather than at aerodynamic control elements (wings and stabilizers), cannot detect a fast growing ice layer until it reaches a sub-mm thickness (>0.2 mm), and are limited in response time (>3 s). The development of small footprint and lightweight, ultrasensitive ice sensors that yet do not disturb the airflow and resist environmental erosion is therefore a clear need in aeronautics icing research.

State-of-the-art nanophotonic sensors rely on the exposure of engineered nanostructured devices such as evanescent-field enhanced waveguides, whispering gallery mode resonators, photonic crystal cavities, or nanoplasmonic structures.[7] However, these devices are not monolithic but made of heterogeneous materials and rely on their nanometer precision design to achieve maximal sensitivities, this implying that they are fragile and rely on careful calibrations, becoming either catastrophically damaged or dysfunctional if systematically exposed to harsh environmental conditions (i.e., contamination, chemical corrosion, erosion, vibrations, and large temperature variations >200 °C). As a result, the goal of designing sensitive surface sensors that can yet sustain long-term operation in harsh environments has hitherto not been achieved.

Here, we demonstrate a harsh-environment-resistant photonic water-ice sensor that probes external molecular changes through resonant light transfer across the infrared OH-stretch vibrational mode, which is a known sensitive probe of the intermolecular distances between water molecules.[8] The sensor was designed on the basis of being resistant to large temperature changes, moderate surface erosion and vibrations, and yet being not-intrusive to aerodynamic flow and highly sensitive to water ice layers. It is based on a mid-infrared (mid-IR) waveguide seamlessly formed inside a transparent glass substrate and low-loss interconnected to external optical fibers for remote optical monitoring. Fast differentiation between water, SCW, and crystalline ice was first evaluated through both numerical simulations and laboratory experiments. To prove the sensor robustness and response in a relevant environment, extensive tests were done in an icing wind tunnel in conditions ranging from in-flight cold rain to fast accretion of different types of microstructured rime and glaze ices. Finally, the tuning of sensitivity to an ultrawide range of water layer thicknesses from sub-mm down to nanometric widths (≤100 nm) was demonstrated by varying the waveguide parameters. Overall, this type of robust and sensitive photonic water-ice sensor could find application in the aircraft industry as well as in other fields where precise monitoring of the phase or composition of water molecules within micro- to nanometric layers is needed, such as for biogenic ice nucleation research, the freeze-drying food and pharmaceutical production, wind turbines, the nuclear fission industry, for in-field medical analysis, in cryogenic high-vacuum space-simulation testing chambers, or for fundamental atmospheric science.[9–15]

2. Sensor Concept and Design

The sensing mechanism of the mid-IR waveguide sensor is 3D rendered in **Figure 1**A. The waveguide follows an in-depth bent path so as to pass several micrometers below the surface to be sensed, and deepens away from it to achieve low-loss direct interconnection with embedded commercial fibers. The phase state of water droplets in the sensing region determines the efficiency and frequency of the resonant transfer condition as a result of the large complex refractive index changes of water around its OH-stretch vibrational fingerprint. The mid-IR waveguide circuit is embedded by means of sub-picosecond multi-scan 3D direct laser writing (3DLW) in commercially available IR-grade fused silica glass ($aSiO_2$), which has well-known mechanical and chemical stability, besides its widespread use in many technologies. Light tunneling can take place even if the sensing waveguide is buried tens of micrometers inside the glass, so that the sensor has the unique feature of being erosion resilient while also being highly specific and sensitive. Figure 1B shows the sensor cross-section scheme and its main design parameters: the core width (W), height (H), and the gap to surface (G). Additional parameters are the waveguide core index difference with the glass surrounding ($\Delta n = n_{core} - n_{aSiO2}$), and the length of the interacting path (L). All these parameters can be tailored at the fabrication stage so as to optimize the sensor for a given application (layer thickness of interest or level of attenuation) as discussed below. Figure 1C shows an experimental image of the waveguide mode near-field intensity at 3.68 μm before it is bonded to optical fibers (see Figure S2.1 and Supporting Information for further experimental details).

3. Sensor Simulations

Several electromagnetic beam propagation simulations based on the beam propagation method (BPM) were carried out to show the waveguide output photon flux as a function of the external medium being air, liquid water at room temperature, or homogenous clear ice at −7 °C using data from Hale[16] and Warren[17] for the index of refraction of water and ice, respectively (see the Supporting Information for further details). Figure 1D shows the obtained field intensity ($|E|^2$) profiles, for a glass sample of 16 mm total length with an interaction (sensing) waveguide length of 2 mm. The waveguide core size is $W = H = 14$ μm, the gap $G = 2$ μm and the refractive index change relative to the silica cladding is $\Delta n = 8 \times 10^{-3}$. These parameters give single mode behavior at wavelengths between 3 and 4 μm (see experimental mode in Figure 1C). It can be clearly observed that the presence of ice induces a strong power attenuation of the guided light due to resonant light tunneling, and which does not occur when water is in liquid state or there is air. The detection principle relies on the evanescent coupling between the waveguide mode and available light modes in the external water layer, a process which occurs most efficiently at a different wavelength depending on the phase state of water and its complex index of refraction.[18] The selectivity of this process also allows to easily distinguish between ice and metastable SCW, which has a maximal structural similarity to ice.[1–3] Figure 1E shows the measured sensor output when the sensor is temperature controlled to perform cyclic freezing and melting phase changes of water droplet on top of the sensor just below and around the freezing point (see the Supporting Information for further details).

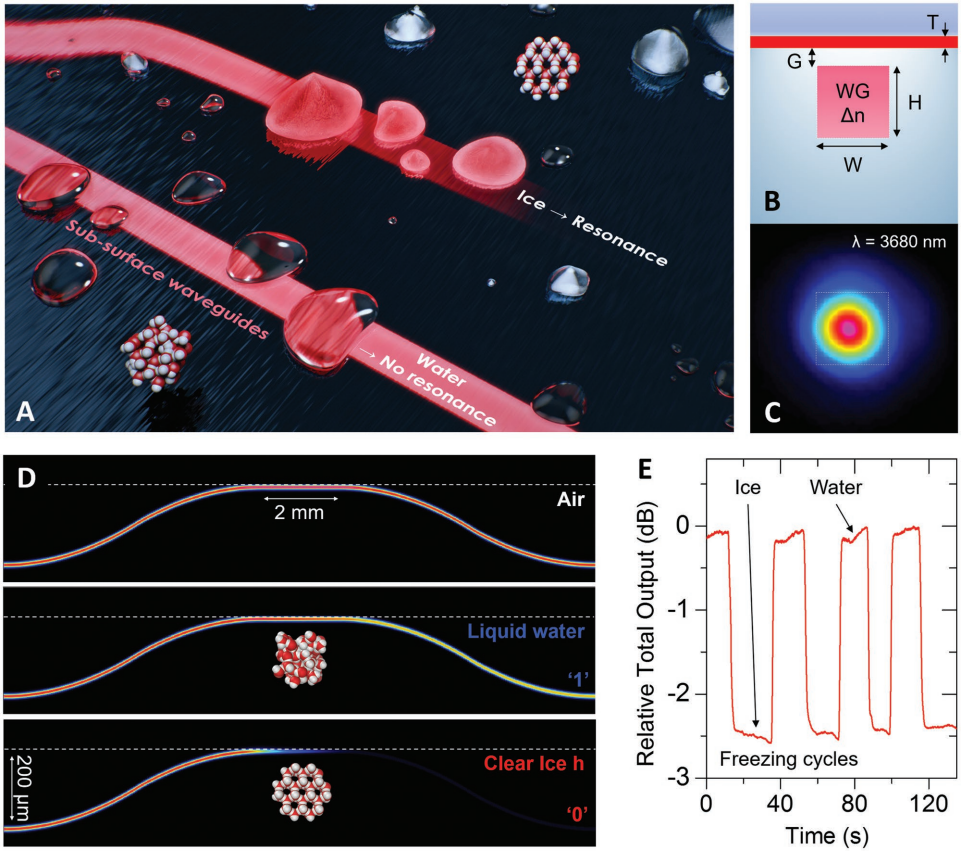

Figure 1. Mid-IR water ice phase surface sensor. A) 3D rendered, conceptual view of the photonic sensor working mechanism. Credit: A. Trujillo. When water droplets are present on the sensor surface detection occurs by means of resonant light transfer to droplets whose index of refraction produces a phase matching condition implying a sudden dip on transmitted light. By spectrally tuning light across the OH vibrational band of water the phase state of the water layer is obtained. Since waveguides propagate below surface the sensor is immune to erosion or scratches smaller than its depth gap. B) Sensor design cross-section parameters (typical values $W = 15$ µm, $H = 15$ µm, and $G = 5$ µm) which can be changed to maximize the light coupling sensitivity to a given layer thickness T (from ≈100 nm to ≈500 µm). C) Measured near-field of the waveguide output at 3.68 µm wavelength. D) Electromagnetic beam propagation simulations of light travelling the 2 mm long sensing waveguide for air, room temperature water, and clear −7 °C homogenous ice surface layers. E) First tests on experimental detection of freezing cycles of a water droplet with the glass sensor temperature controlled by a peltier unit and detection with a thermal power meter. The measured output intensity is evaluated as relative output power (dB) between ice and liquid water states.

Since the waveguides have a low index contrast to surrounding glass (less than 1%),[19] the effective index of the waveguide mode is only marginally higher than the refractive index of fused silica and phase matching regions can be first identified by evaluating the spectral dispersion of the complex index of refraction of all involved materials. **Figure 2**A shows the index of refraction n and extinction coefficient k dispersion values for $aSiO_2$ glass,[20] clear ice at −7 °C,[17] and liquid water at 25 °C[16] in the 2.6–4 µm wavelength region across the OH-stretching vibrational mode of water. Resonant light transfer is allowed for wavelengths where the n index matching condition is fulfilled (≈3.46 µm for warm water and ≈3.68 µm for −7 °C clear ice), while the extinction coefficient is low ($k \leq 10^{-2}$). At shorter wavelengths where the anomalous dispersion of water takes place (≈3 µm) no light transfer occurs due to the large water k increment of almost two orders of magnitude.[18] To fully evaluate these assumptions, wavelength sweeps of BPM simulations of the sensor response across the 3–4 µm wavelength range were performed with the sensor surface covered with infinite thickness layers of air, water, or ice, which allows to qualitatively evaluate the sensitivity of the device to liquid/solid phase transitions of water (see Figure 1D as BPM example for $\lambda = 3.62$ µm light), and the expected spectral response across the anomalous-to-normal water dispersion range. Figure 2B shows the sensor spectral output response for ice and water layers (normalized to air and per mm of sensing length) and for sensing waveguides of low (Δn^L) and high index change (Δn^H). The parameters for Δn^H are the same as those for Figure 1D, and the parameters defining the waveguides for the Δn^L case are $W = H = 28$ µm, $G = 5$ µm, and $\Delta n = 2 \times 10^{-3}$, which result in the same waveguide normalized V number (1.89)[18] associated to the Δn^H waveguides, so that direct comparison can be made. A set of simulations with $\lambda = 3$ µm to $\lambda = 4$ µm have been implemented in order to determine the optimum wavelength (i.e., perfect index matching conditions) at which the power attenuation is maximum when ice is formed on the surface. As seen in Figure 2B, maximal light attenuation when ice forms at −7 °C happens at around 3.68 µm as expected before

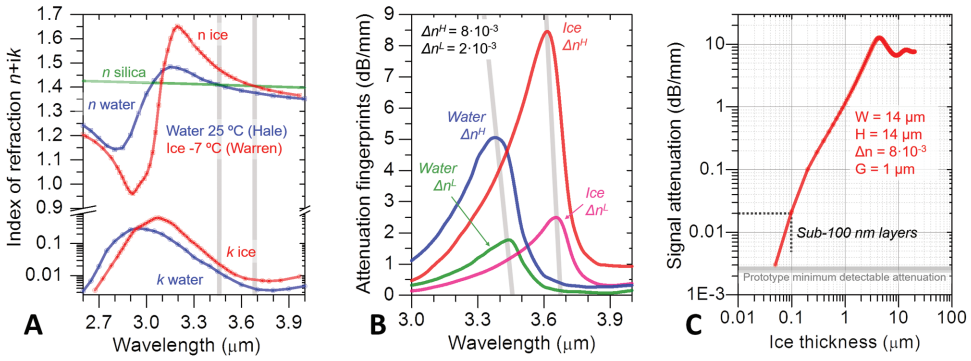

Figure 2. Directional coupling (light tunneling) conditions and simulation of sensor performance across the anomalous-to-normal dispersion range of water. A) Complex refractive index of liquid water (25 °C) from Hale[16] and ice at −7 °C from Warren[17] and index of refraction of fused silica glass. The phase matching wavelengths between water and silica are indicated with gray vertical bars at around 3.46 μm (liquid water) and 3.68 μm (ice). B) Simulated sensor spectral output response for ice and water layers (normalized to air and per mm of sensing length). For small gaps ($G < 5$ μm), the differential attenuation levels (sensitivity) between ice and water depend on the waveguide refractive index change Δn, due to the change in waveguide propagation constant. No light tunneling occurs across the 3 μm wavelength region due to the two orders of magnitude increase of the imaginary part $k(\lambda)$ of the complex index of refraction of water (see (A)). C) Simulation of sensor output attenuation as a function of ice layer thickness in water. Maximum attenuation occurs for single mode ice layers of around 3 μm thickness. Due to the large differential absorption of liquid water and ice the sensor can also detect formation of nanometric (100 nm) ice layers below liquid water (the minimum detectable attenuation with our experimental setup is of 0.0026 dB, given our SNR of 32 dB. See the Supporting Information for further details).

from Figure 2A, but at slightly lower wavelengths of 3.62 μm for the Δn^H case, and 3.65 μm for Δn^L due to the increase of the mode effective index with respect to bulk silica. The spectral attenuation corresponding to room temperature liquid water as external medium also peaks at around the expected wavelength of 3.46 μm from Figure 2A, but again slightly blue-shifted due to the higher values of mode effective index with respect to bulk silica. These results demonstrate the impact of the waveguide index contrast on the sensitivity and selectivity of the sensor to ice and liquid water. For a higher sensitivity and selectivity, higher contrast waveguides are required, at the cost of a reduced gap (G) which can make the sensor weaker in harsh environments due to a reduced erosion resistance.

All previous simulations were done for infinite layer thicknesses, so that no evaluation of the sensor response against layer thickness was performed. To evaluate this, layer thickness simulation sweeps were performed for various sensor configurations (see Figure S1.12, Supporting Information). The attenuation levels (in normalized dB mm^{-1} units) for ice layers against water are shown in Figure 2C for the case of a sensor with small gap G = 1 μm and Δn^H. The sensor surface was covered by room temperature water and layers of ice with decreasing thickness (T) from 20 μm down to 50 nm were computed. Maximal attenuation is obtained for ice layer thickness of micrometer size around the wavelength size (12.6 dB mm^{-1} for $T \approx 4$ μm) with an oscillating behavior as T increases, due to the creation of a higher number of modes available on it, stabilizing at around 7.5 dB mm^{-1} for $T \geq 20$ μm. Toward the nanometer range the sensitivity for ice against water decreases reaching a computed value of ≈0.02 dB mm^{-1} attenuation for ice layers of 100 nm thickness. This small attenuation level in the output signal is ≈8 times above the experimentally determined minimum detectable attenuation (≈0.0026 dB) given by the detection noise floor of our prototype (SNR of ≈32 dB, so that we can detect signal attenuations as small as ≈0.06%; see the Supporting Information for further details), so that this type of sensor could also be used for fundamental studies of nanometer confined water dynamics, although this goes beyond the scope of this report where we focus only on micrometer scale icing.

4. Sensor Laboratory Proof of Concept

The experimental development of a sensor laboratory prototype was initiated using 3DLW low contrast waveguides, which allowed for the proof-of-concept demonstration under static water layer conditions in an optical bench with the sensor itself as temperature changing element. Three mid-IR lasers were used, a tunable OPO for broad wavelength tuning from 3.3 to 3.7 μm, a He-Ne gas laser at 3.39 μm, and an ICL diode at 3.68 μm (see the Supporting Information for further details). High-contrast waveguides, which were experimentally developed later on (see ref. [19]), were integrated in a wing mock-up model for dynamic icing wind tunnel tests for simulation of in-flight aircraft icing conditions. The first goal of experimental developments was the verification of the simulated attenuation spectral fingerprints of room temperature liquid water and clear ice (see Figure 2B), as well as of metastable SCW layers. For these experiments, a waveguide with the following parameters was used: W = 32 μm, H = 15 μm, G = 6 μm, and an estimated $\Delta n = 2 \times 10^{-3}$. The total waveguide length was 18.2 mm, but deionized water droplets with diameter of only a few mm were used. The experimental setup with a tunable mid-IR OPO laser is shown in Figure S2.1 (Supporting Information), for which static droplet measurements were recorded by covering the chip with a mm-sized water droplet, stabilizing the temperature of the surface at a given value, and running a fast laser wavelength sweep of a few seconds from 3.3 to 3.7 μm in order to obtain a spectral water fingerprint at that given temperature and water phase. To obtain SCW, cyclic droplet freezing/melting steps were done, so that measurements at a

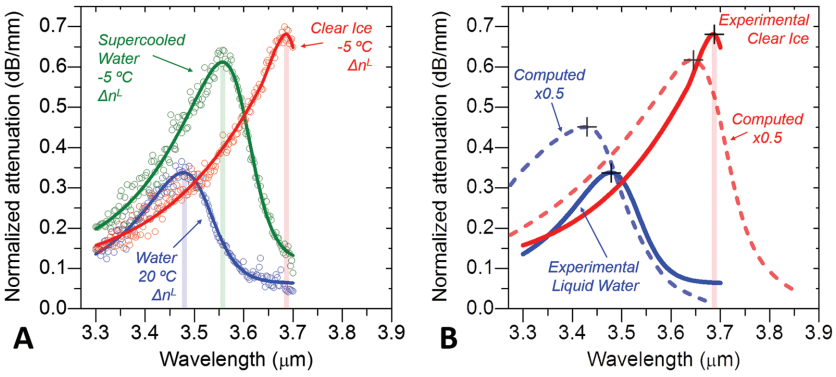

Figure 3. Experimental spectral fingerprints for warm water, SCW, and clear ice with a low contrast (Δn^L) waveguide sensor. A) Experimental normalized attenuation spectra for deionized water drop at 20 °C (blue data), and at −5 °C for both its SCW (green data) and solid state (red data). Solid lines are best fits to experimental points. Data noise is mostly arising from random output power oscillations of the tunable mid-IR OPO laser used for the experiments. Peak attenuation wavelengths are marked for each water phase state. B) Evaluation of the matching between experimental normalized attenuation sensor data (asymmetric peak fits) and BPM simulations. Experimental data is the same as in (A), simulations used same water index of refraction data as in Figure 2, and normalized attenuation is divided by 2. Good qualitative agreement on the powerful selectivity on ice against water is found, which validates the sensor 3DLW fabrication technique.

same nominal temperature could be repetitively performed for both metastable and solid phases before transitions occurred. All output spectral measurements were normalized to an air reference obtained previously at the same nominal temperature, so that potential chromatic effects associated with the whole opto-mechanic and photonic system were removed. The raw normalized attenuation results as well as their fits to asymmetric double sigmoidal peaks are shown in **Figure 3**A. The noise in the data arises from the output power fluctuations when sweeping the OPO laser wavelength. At 3.68 μm wavelength, a maximal selectivity of 0.54 (0.60) dB mm^{-1} between −5 °C solid ice and −5 °C SCW (20 °C warm water) is found. The spectral fingerprint of SCW (green data) resembles a water structure in between normal liquid water and ice, with a large peak red-shift of ≈80 nm with respect to 20 °C water due to its structural similarity with ice, although solid ice peaks with a further red-shift of ≈130 nm from SCW, clearly depicting the higher crystalline order and associated polarizability change at the OH-stretch vibrational resonance which drives the large index change (see Figure 2A). In order to evaluate the validity of BPM computations, a simulation set was performed for the exact waveguide parameters of Figure 3A, and which is shown in Figure 3B, using the same complex index of refraction data as in Figure 2. For the sake of visual comparison all attenuation values for the simulation results are divided by 2, so that one of the first conclusions is that at least for the low contrast waveguides (Δn^L), relative attenuation values between ice and water are overestimated by an order of ≈2 or lower. Besides this, a very good qualitative agreement is found in the ice/water fingerprints, although it is worth noting that a much better agreement is found for −5 °C ice than for 20 °C liquid water. There are many factors that can explain the found discrepancies, such as the mismatch between used dispersion data from Warren and Hale for simulations and real values, nonperfect modeling of the photonic structure (e.g., inaccurately estimated Δn) or defects in the fabrication along the waveguide. An in-depth refinement of these issues is currently in development.

Once the experimental spectral fingerprints of each water phase were determined, the temporal response of the sensor was studied at three different wavelengths: 3.39, 3.64, and 3.68 μm. The initial sensor tests were performed at 3.64 μm wavelength with an OPO laser system, and the output power measurement was done with a thermal power meter. Fast liquid–solid phase transitions of a 5 mm long water droplet were performed in a laboratory sensor configuration with low thermal inertia (i.e., direct contact between a peltier unit and the sensor glass chip; see the Supporting Information), and in the surface temperature range from −5 to +5 °C calibrated with a FLIR thermal imaging camera. These experiments were performed first freezing the whole droplet until its top tip, and afterward cycling the sensor temperature preventing the full frozen droplet from becoming liquid entirely, that is, with only the droplet surface contact area melting before the temperature was again decreased so freezing occurs within seconds and cycles were of around 40 s. Figure 1E shows this water phase change cycling at 3.64 μm wavelength.

In a second round of tests at 3.68 μm wavelength with an ICL, the configuration was slightly modified: direct laser coupling of light was done by means of bonded optical fibers and the glass sensor chip was attached with thermal silver paint on a thick piece of metal which added thermal inertia to the system. In this experiment, the sensor response when a room temperature (+20 °C) liquid water drop is slowly cooled to −20 °C is monitored. **Figure 4**A shows the evolution of the temporal power loss with respect to the uncovered sensor. The 0 s time is set when temperature started to decrease at around 20 °C min^{-1}. It can be observed that signal starts to decrease for colder water as it was also seen in the recorded spectrums of Figure 3A. At some point a sudden fall of the signal (of about 0.35 dB mm^{-1}) indicates the liquid–solid phase transition at freezing point. Figure 4A shows the detail of this transition, where it can be seen that its apparent duration is measured to be of ≈300 ms, although this is a response time given by the used electronics and signal processing system.

A third set of freezing drop experiments was performed with a fiber-coupled sensor prototype inside a freezing chamber, so that the same transition as in Figure 4A could be done instantaneously. This prototype was integrated on the leading edge of a 3D printed wing model for ice detection in real in-flight icing conditions (see Figure S2.7 and Supporting Information). In this prototype 3DLW waveguides had a high contrast (Δn^H). Specifically, the core parameters were $W = 13$ μm, $H = 13$ μm, an estimated $\Delta n = 8 \times 10^{-3}$, and $G = 4$ μm. Before sensing tests, the waveguide technology and its optical bonding to fibers had to be tested at low temperatures and for large and fast temperature changes. The sensor was first continuously tested at −30 °C for 24 h, without observing any change in its output signal levels,

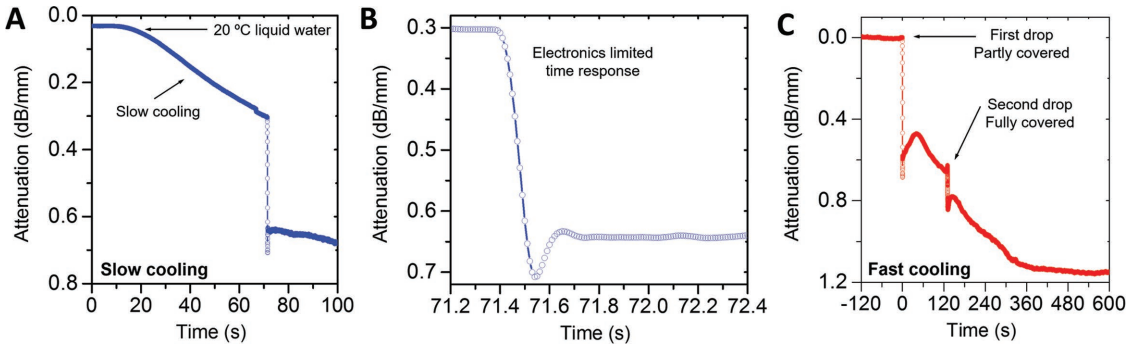

Figure 4. Characterization of the sensor prototype response time. A) Time record in slow cooling and freezing of a room temperature +20 °C liquid deionized water droplet down to −20 °C. B) Detail of the time response at the freezing point of the water-sensor surface area. The response time is given by the electronics slow response, of around ≈300 ms. C) Time record of fast cooling experiment for +20 °C deionized water droplets when in contact with the sensor at −15 °C temperature, inside a freezer chamber. Two droplets were used, a first one which covered around 75% of the sensor surface, and a second droplet covering the remaining sensor area. The sensor response time at the freezing transitions has the same electronics limited time response as in slow-cooling experiments, proving that the sensor response can be improved by using faster electronics and signal analysis.

and afterward was exposed to fast temperature changes performed by moving the sensor from inside the freezer at −30 °C to a water bath at +20 °C. Once the sensor prototype resistance to temperature changes and low temperatures were verified, tests were performed inside the freezer. In this case, the sensor was fully maintained at −15 °C, and drops of warm deionized water at +20 °C were dropped on it. Figure 4C shows the time signal evolution, in which the 0 s time is set when the first drop contacts the sensor. First, a small water drop (covering around 6 mm of the sensor) freezes instantaneously in its bottom in contact with the cold sensor and produces the first strong signal drop (of ≈60% signal, or 0.6 dB mm^{-1}). Second, another drop fills the rest of the sensor and the signal goes further down by around −0.2 dB mm^{-1} more, being followed by a very slow signal drift probably due to the gradual cooling of the whole ice layer down to −15 °C of the freezer environment. The results of Figure 4C corresponding to the second sensor prototype sensing clear ice at −15 °C will be later compared to results from the icing wind tunnel tests, labeled as laboratory clear ice reference.

So far, only homogeneous ice (i.e., no air microbubbles inside) has been considered. However, aircraft icing typically takes place in mixed conditions, where ice layers feature a heterogeneous microstructure with air grains of variable size, giving rise to different types of phenomenological macroscopic ice types such as frost or rime ice. These microstructured ices are characterized by a nonhomogeneous microstructure which will therefore have different optical properties and affect the sensor's principle of operation. A simple model was used to simulate rime ice consisting of ice and air blocks with average lengths along the light propagation direction of 80 and 20 µm. The ice blocks had a thickness of 50 µm and an infinite width perpendicular to the propagation direction. As before, the attenuation spectrum was calculated and the comparative results between liquid water, ice, and frost/rime can be seen in **Figure 5**A. Note that here we refer to rime or frost ices as similar cases of microstructured ice (air and ice grains with any given volume filling fractions, sizes, and distributions), even if these are terms for types of ices which

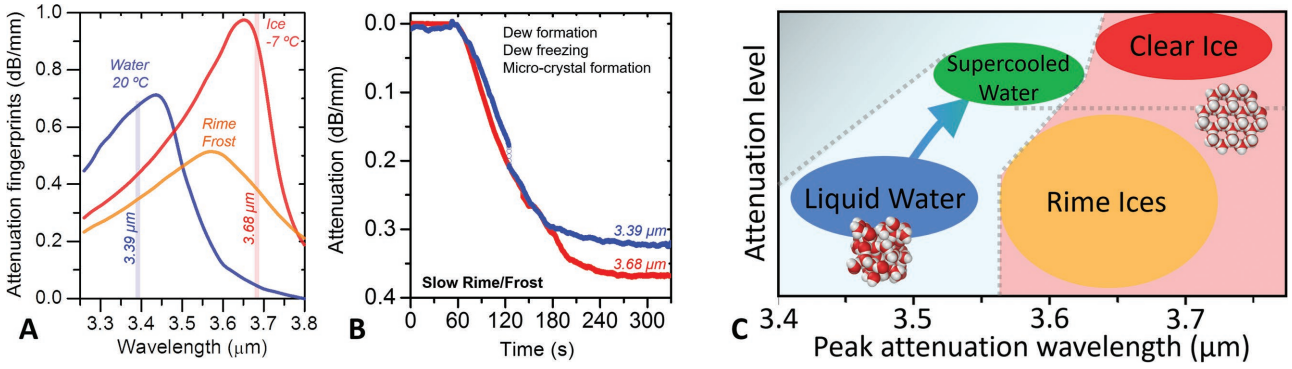

Figure 5. Simulation and experimental formation of frost microstructured ice. A) Simulation of liquid water, homogenous clear ice, and air/ice microstructures (frost/rime). Microstructured ice is clearly identified by an increased full width at half maximum of its attenuation fingerprint and a peak intensity reduced to around a 50% with respect to homogenous clear ice. B) Experimental time response of the sensor for the slow formation of frost by first allowing dew to condense at room temperature conditions and slow sensor cooling, dew freezing, and ice microcrystals formation across the sensor area. Good agreement for attenuation values at 3.39 and 3.68 µm is found between simulation (A) and experiments (≈0.35 dB mm^{-1}). C) Conceptual sketch on the sensor response parameter space–attenuation peak level against wavelength, and the different regions corresponding to each water phase and microstructured rime ice types. A third parameter (not shown here) is the spectra full width at half maximum, which allows to differentiate between homogeneous (liquid or solid water) and microstructured ice (rime or frost) (see (A)).

form in completely different circumstances and physical parameters. The main differences of the simulated sensor attenuation output spectra for rime/frost curve with respect to the ice and water curves are that its peak wavelength is located in between the other two maximums (at $\lambda \approx 3.58$ μm), that this maximum value is lower than all other water phases or states, and that the resonance has a very damped behavior with a very large full width at half maximum, probably caused by the presence of the air blocks which induce scattering in the ice/air interfaces. Depending on the ice microstructure the attenuation spectrum can therefore vary substantially, but ice microstructures with air pores are clearly identified by a strong fingerprint blue-shift with respect to homogenous clear ice and a low attenuation value as well as very large width. To simulate this type of microstructured frost-like ice in the laboratory a series of experiments were performed using the same setup as for slow water cooling (see Figure 4A). Frost ice was created on the surface by slowly cooling down the sensor at room temperature, allowing dew formation due to vapor water condensation. At a given time, the dew freezes, and ice microcrystals (frost) start to grow (see Figure 5B). In this condition and within a few minutes, ice crystals had grown to enough size to be seen by the naked ice, showing the characteristic white aspect of frost. This experiment was performed in the laboratory for the wavelengths of 3.39 and 3.68 μm, which lie both out of the maximal fingerprint attenuation. The two independent experiments were performed under the same protocol and are plotted on the same time scale in Figure 5B. The initial and final temperature is 20 and −15 °C, respectively. Both curves show a gradual fall of the output power which corresponds to freezing of the dew across the sensor surface area, as well as a saturation region at the end indicating no further growth of microcrystals on the glass surface. A very good agreement is found between experiments and rime-frost simulation (Figure 5A), with attenuation levels of around ≈0.35 dB mm^{-1} for both wavelengths, and slightly higher at the longer wavelength of 3.68 μm.

Overall, these findings demonstrate that these novel types of mid-infrared water ice sensor allow to clearly distinguish between the structural phases of water, as well as its microstructure with regard to rime-type or frost structures with given percentages of microporosity. The main detection parameters to effectively identify these different icing conditions are the operating wavelength (which allows to tune the sensor for an improved selectivity of a given water phase against other) and the attenuation values spectral dependence. A clear trend is observed for which liquid water is detected for wavelengths gradually shifting from ≈3.45 μm (+20 °C) to ≈3.55 μm (−5 °C, metastable SCW), clear ice peaks at much longer wavelengths ≈3.68 μm and with higher attenuation levels, and rime ices do peak in a wide region between SCW and clear ice, but with a reduced attenuation to half the level of clear ice. These observations are summarized in a hypothetical parametric table in Figure 5C. To fully confirm this sensor capability further experiments must however be performed under more sophisticated experimental conditions covering the whole range from liquid to solid water, as well as microstructured ice types with varying air pore densities from low to high density rime ices.

5. Sensor Prototype for Icing Wind Tunnel Tests

To further prove that this sensor can operate in harsh in-flight conditions, under high speed water impact, and at low temperatures, we performed a series of tests inside an icing wind tunnel (IWT) at the Fraunhofer IFAM icing facilities (see Figure S2.6 and Supporting Information). The sensor prototype used is the same as that tested in freezing conditions as previously described (see Figure 4C). Regarding the icing testing facility, it consisted of a wind tunnel capable of simulating dangerous in-flight icing environments, such as clouds being composed of supercooled water droplets, and where wind speed, temperature, liquid, and water droplet size could be accurately controlled. The sensor mock-up was first tested at various temperatures at 55 m s^{-1} speeds, in order to check that there were no material failures after prolonged use (3 h continuous test). Signal stability and repeatability between air, water, and ice cycles was very high. The temperatures to test were +10, 0, −15, and −30 °C (±2 °C), the wind speeds were of 55 and 95 m s^{-1}. The liquid water content (LWC) was of 2.1 and 0.8 gr m^{-3}, for 55 and 95 m s^{-1}, respectively. Mean droplet volume diameter (MVD) was of 40 μm. **Figure 6** shows the visual appearance of the leading edge of the wing model where the sensor was embedded, 3 s after the cloud was created. The sensing waveguide was driven by the ICL diode at its nominal wavelength (3.68 μm) and the output signal was measured by the PbSe detector (see Figure S2.10 and Supporting Information for further details). The temporal evolution of the sensor's output signal is depicted in **Figure 7**A, where relative output power values are given in dB for the whole sensor waveguide length of 8 mm. At temperatures above the freezing point, the signal output power decreases by a very small margin. A noise component is added to the signal indicating the impact of the water droplets on the glass surface, which is more evident at 55 m s^{-1} than at 95 m s^{-1}, probably meaning that in the latter case a continuous film of water remains on the surface. In the opposite case, when the temperature is well below 0 °C (at −15 and −25 °C), the output signal quickly falls around 10 dB within 1 s as a consequence of ice accretion. At 3.68 μm wavelength, the detection of ice is therefore characterized by a clear and fast signal attenuation, of the order of 10 dB. However, this attenuation level evolves to a steady state more characteristic of microstructured rime ice, with a lower attenuation value of around 7 dB. Finally, at temperatures around the freezing point, the sensor response differs in its slow response. Although not immediately, the signal still decreases more than when having positive temperatures and hence icing conditions might be inferred. A plausible explanation for this is the fact that small fluctuations of temperature around ±2 °C could prevent locally the water droplets from freezing on the glass surface, resulting in a mix of ice-water millimeter-sized films. In any case, the sensor can clearly detect when there is running water (droplets impact) from the measured noise fluctuations, and in the case that an ice layer is blocking the sensor is so identified by the absence of noise. By using the ice sensor in conjunction with de-icing electrothermal systems which could fast remove any detected ice layer icing safety would therefore be largely increased.

The attenuation values in the steady state for each IWT test were also measured at three different wavelengths. Although

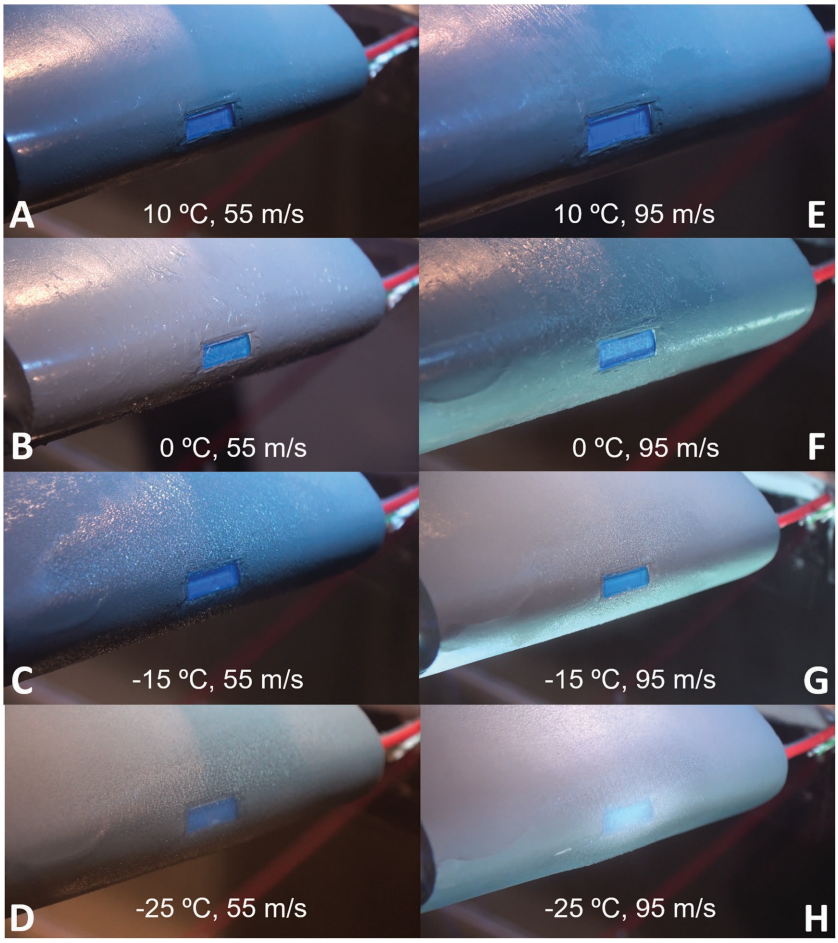

Figure 6. Wing model leading edge appearance for various temperatures and wind speeds inside the IWT. Only in the case of –25 °C and 95 m s^{-1} air speed can the first layers of icVe be detected by the naked eye.

the ICL laser is not continuously tunable, three current–temperature set-points that provided single-frequency lasing (3.60, 3.64, and 3.68 μm) were used. In Figure 7B, the final steady states are summarized and compared with homogenous clear ice detection in a freezing chamber (see Figure 4C) as a reference for –15 °C clear ice. All the ice films created inside the wind tunnel produced a different spectral sensor response from the one corresponding to the reference ice. In general, the lower attenuation observed at any of the spectral points, the higher proportion of low-density rime-like microstructured ices present on the sensor surface. In our experimental set of icing parameters, temperature was the dominant factor, having the ices accreted at –25 °C a less dense nature than those at –15 °C. At 55 m s^{-1} speeds, high-density microstructured ice formed only at –15 °C temperature (orange line), which gave a fingerprint very similar to that of clear ice but with decreased attenuation at 3.68 μm wavelength, while lower density microstructured ice (with milky appearance as seen by the naked eye) with reduced attenuation formed at –25 °C (gray line). At 95 m s^{-1} speeds a similar trend can be observed to occur: high-density and slightly lower density microstructured ices also formed for –15 and –25 °C temperatures, respectively; and with similar attenuation values to 55 m s^{-1}. At the freezing points (0 °C), all attenuation curves correspond to cold liquid water. The reason for this is that the values were taken in a

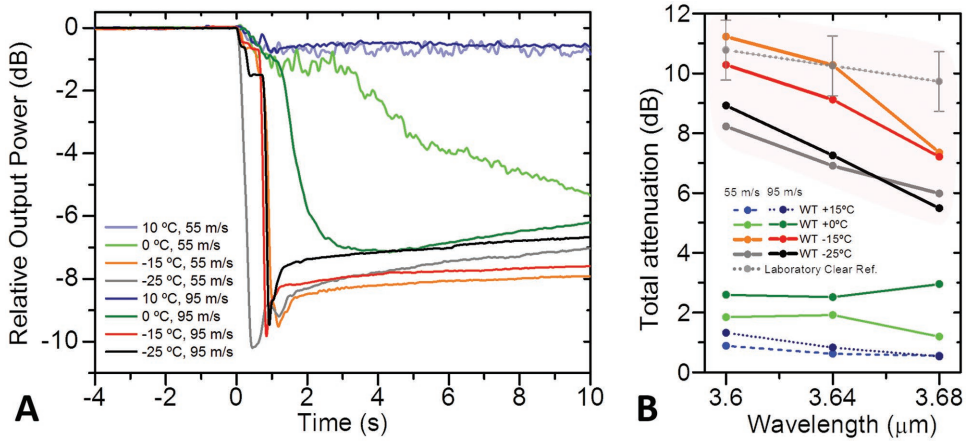

Figure 7. In-flight icing detection. Icing wind tunnel tests. A) Time signal detection at +10, 0, –15, and –25 °C (±2 °C) and wind speeds of 55 and 95 m s^{-1}. Fast micrometric ice layer accretion is detected in less than 1 s. Afterward, ice layers evolve toward a steady state depending on the air temperature and wind speed. At freezing point temperatures, a thin ice layer forms slowly at a time scale of around 4–20 s, and afterward gradually melts within various minutes (not shown for the sake of brevity). Above freezing temperatures only impacting drops are measured which produce an oscillating signal with almost no attenuation. B) The final steady states are summarized and compared with homogenous clear ice detection—out of the wind tunnel—in a freezing chamber (see Figure 4C) as a reference for –15 °C clear ice.

stationary regime when the output power had increased relative to the initial sudden fall. Such increase is probably due to high speed water droplet impacting on the sensor surface and detaching the first layer of accreted ice before forming a thin layer of very cold liquid water film below an igloo-like ice structure surrounding the sensor area. We therefore show here that the ice contact surface layer can fundamentally change in subsecond time scales, and this type of sensor can continuously monitor these changes, thus enabling the development of future fast-response automated active de-icing electrothermal systems.

6. Conclusions

In conclusion, we have introduced a novel concept for photonic surface sensors capable of withstanding harsh environments and yet be sensitive enough to detect water molecule phase changes with layer thicknesses within the micrometer scale and nanometric scale. The concept has also been fully developed in prototypical form and tested on industrially relevant environments, such as in icing wind tunnel for replicating in-flight icing conditions. We have shown that this novel type of mid-infrared sensors can be exploited for detecting both structural phase changes of water, as well as microstructural arrangements of porous ices such as rime ice, which pose a serious threat to aircraft transport. Furthermore, the use of silica glass as surface sensor allows opening various research avenues which could have a strong impact in both applied and fundamental sciences. An opportunity opens for studying the sensor behavior in combination with hydrophobic or icephobic microstructured surface ends. In a similar way to how the sensor detects microstructured ice with air pores, the detection of water or biological matter in contact with microstructured silica could be investigated, for which the sensor would perform as an element of inbuilt monitoring capability for the automated feedback control of other systems. Additionally, biofunctionalizing the SiO_2 sensor surface[20] would also enable to exploit the sensor in the novel field of mid-infrared biosensors. In parallel, the current rapid development process of mid-infrared photonic technology (such as tunable or supercontinuum laser sources, optical fibers, and detectors) will undoubtedly lead this type of glass embedded surface sensors of a wide range of scientific and engineering applications.

7. Experimental Section

Sensor Simulations: BPM simulations of the waveguide sensor performance were carried out by means of the commercial RSoft BeamPROP software package. Complex refractive index dispersion data were taken from refs. [16], [17] and [20] for liquid water at 25 °C, ice at −7 °C, and fused silica, respectively. The geometry of the structure was parametrized according to Figure 1B and Figure S1.1 (Supporting Information). Only scalar simulations were performed as the sensing performance did not depend on the light polarization. In all cases, the excitation field was the waveguide's own fundamental mode. For the broadband results presented, individual simulations at different wavelengths were carried out taking into account the optical dispersion of materials. Extensive details about all the aspects of the simulations can be found in Part SI (Supporting Information).

Photonic Sensor Fabrication: The waveguides were fabricated using the 3DLW multiscan technique on commercial low-OH fused silica glass substrates (Suprasil 300). For the low contrast waveguides (estimated $\Delta n^L \approx 2 \times 10^{-3}$), a 1033 nm wavelength, circularly polarized laser beam, giving 400 fs pulses with an energy of 0.5 μJ at a repetition rate of 500 kHz was focused inside the sample trough an aspheric lens of 0.25 NA. The sample was translated at a speed of 1 mm s^{-1} to produce rectangular cores with $\approx 32 \times 14$ μm^2 size. For the high contrast waveguides, the fabrication parameters were, respectively, 1047 nm laser wavelength, circular polarization 450 fs pulse width, 0.9 μJ pulse energy, 500 kHz repetition rate, 0.4 NA, and 1.5 mm s^{-1} scan speed. The obtained waveguide core had a size of around 13×13 μm^2 with an estimated $\Delta n^H \approx 8 \times 10^{-3}$ at 3.68 μm wavelength. Further details about the fabricated waveguides were reported elsewhere.[19] After the 3DLW process, the samples were physically polished to reduce the waveguide-surface gap to the desired values. Bonding the waveguides to mid-IR ZBLAN cleaved fibers was done using optical adhesive NOA 61. The connection area was covered by adhesive prior to carefully aligning the cleaved facets of the fibers with the corresponding ports of the waveguide. UV light was then applied to cure the adhesive and make a permanent connection. For the integration of the sensor on an aircraft structure, a wing mock-up (NACA 0012) 3D printed in PLA was properly modified to host the glass substrate on the leading as well as the optical fibers. See further details in Part SII (Supporting Information).

Sensing Experiments: Ice sensing demonstration in an optical laboratory was carried out in a standard optical waveguiding setup for mid-IR guiding. The sources used were a Firefly-IR OPO (M Squared Lasers), a 3.68 μm ICL laser (Nanoplus), and a 3.39 μm He-Ne laser (REO). The detectors were a Thorlabs S302C thermal power meter, a Thorlabs PDA20H-EC PbSe amplified detector, and a FLIR SC7000 InSb camera. For free-space experiments, a pair of chalcogenide aspheric lenses with NA = 0.18 (Thorlabs C021TME-E) coupled the light in and out the waveguide, respectively. A peltier unit controlled the temperature of the sensor while the temperature was constantly monitored by a calibrated thermal camera. The setup was enclosed in an N_2-purged PMMA chamber to avoid water vapor condensation on the photonic chip facets. In the fiber-coupled case, this was not needed. The ZBLAN fibers used were provided by FiberLabs and Thorlabs and their core size and NA closely matched that of the 3DLW waveguide coupling light into it in order to achieve low coupling losses. For collecting light out of the waveguides, a multimode fiber was used instead. The precise protocol followed to characterize the sensor performance in the optics laboratory and the IWT is explained in detail in Part SII (Supporting Information).

Supporting Information

Supporting Information is available from the Wiley Online Library or from the author.

Acknowledgements

This work was funded by the European Union's Seventh Framework Program for research, technological development and demonstration, Japanese-European De-Icing Aircraft Collaborative Exploration project (JEDI ACE, http://www.jediace.net/) under Grant Agreement No. 314335, and the Japanese Ministry of Economy, Trade and Industry. This work was also supported by the Spanish MINECO and FEDER (MAT2016-75716-C2-1-R), Spanish Ministry of Economy, Industry and Competitiveness (TEC2014-55948-R and TEC2014-52642-C2-1-RF), and Generalitat de Catalunya (2014SGR1358). A.R. and R.O. acknowledge that the research leading to these results also received funding from LASERLAB-EUROPE (Grant Agreement No. 654148, European Union's Horizon 2020 research and innovation programme). F.D. acknowledges additional support 2010-ICREA-02 for excellence in research. A.R.

acknowledges funding from the European Union's Horizon 2020 research and innovation programme under the Marie Sklodowska-Curie Individual Fellowships Grant Agreement No. 747055.

Conflict of Interest

The authors declare no conflict of interest.

Keywords

harsh environments, ice, mid-infrared, sensors, water

Received: April 4, 2017
Revised: April 26, 2017
Published online: June 13, 2017

[1] a) O. Mishima, H. E. Stanley, *Nature* **1998**, *396*, 329; b) J. R. Errington, P. G. Debenedetti, *Nature* **2001**, *409*, 318; c) F. Mallamace, C. Branca, M. Broccio, C. Corsaro, C.-Y. Mou, S.-H. Chen, *Proc. Natl. Acad. Sci. USA* **2007**, *104*, 18387; d) B. Pamuk, J. M. Soler, R. Ramírez, C. Herrero, P. Stephens, P. Allen, M.-V. Fernández-Serra, *Phys. Rev. Lett.* **2012**, *108*, 193003; e) C. Colosi, M. Costantini, A. Barbetta, C. Cametti, M. Dentini, *Phys. Chem. Chem. Phys.* **2013**, *15*, 20153; f) F. Mallamace, C. Corsaro, H. E. Stanley, *Proc. Natl. Acad. Sci. USA* **2013**, *110*, 4899; g) A. Nilsson, L. G. Pettersson, *Nat. Commun.* **2015**, *6*, 8998; h) P. Gallo, K. Amann-Winkel, C. A. Angell, M. A. Anisimov, F. Caupin, C. Chakravarty, E. Lascaris, T. Loerting, A. Z. Panagiotopoulos, J. Russo, J. A. Sellberg, H. E. Stanley, H. Tanaka, C. Vega, L. Xu, L. G. M. Pettersson, *Chem. Rev.* **2016**, *116*, 7463; i) L. G. M. Pettersson, R. H. Henchman, A. Nilsson, *Chem. Rev.* **2016**, *116*, 7459.

[2] a) E. Mayer, A. Hallbrucker, *Nature* **1987**, *325*, 601; b) B. J. Murray, D. A. Knopf, A. K. Bertram, *Nature* **2005**, *434*, 202.

[3] F. Frank, *Nature* **1946**, *157*, 267.

[4] a) S. M. Jones, M. S. Reveley, J. K. Evans, F. A. Barrientos, NASA/TM-2008-215107, USA, **2008**; b) P. Appiah-Kubi, *Master These*, University of Tennesse, USA, **2011**; c) In 2014-25789, Vol. *79* FR 65507 (Ed: F. A. Administration), Federal Aviation Administration, USA **2014**, p. 65507.

[5] S. Jung, M. K. Tiwari, N. V. Doan, D. Poulikakos, *Nat. Commun.* **2012**, *3*, 615.

[6] a) S. Kimura, Y. Yamagishi, A. Sakabe, T. Adachi, M. Shimanuki, *SAE Technical Paper* **2007**; b) J. C. Bird, R. Dhiman, H.-M. Kwon, K. K. Varanasi, *Nature* **2013**, *503*, 385; c) K. Morita, H. Sakaue, T. Tanaka, T. Yoshida, N. Rehfeld, A. Brinkmann, K. Lummer, G. Pauly, *SAE Technical Paper* **2015**; d) K. Golovin, S. P. Kobaku, D. H. Lee, E. T. DiLoreto, J. M. Mabry, A. Tuteja, *Sci. Adv.* **2016**, *2*, e1501496.

[7] a) M.-C. Estevez, M. Alvarez, L. M. Lechuga, *Laser Photonics Rev.* **2012**, *6*, 463; b) C. Fenzl, T. Hirsch, O. S. Wolfbeis, *Angew. Chem., Int. Ed.* **2014**, *53*, 3318; c) Y. Zhi, X. C. Yu, Q. Gong, L. Yang, Y. F. Xiao, *Adv. Mater.* **2017**, *29*, 1604920.

[8] F. Perakis, L. D. Marco, A. Shalit, F. Tang, Z. R. Kann, T. D. Kühne, R. Torre, M. Bonn, Y. Nagata, *Chem. Rev.* **2016**, *116*, 7590.

[9] R. Pandey, K. Usui, R. A. Livingstone, S. A. Fischer, J. Pfaendtner, E. H. Backus, Y. Nagata, J. Fröhlich-Nowoisky, L. Schmüser, S. Mauri, *Sci. Adv.* **2016**, *2*, e1501630.

[10] S. L. Nail, S. Jiang, S. Chongprasert, S. A. Knopp, *Development and Manufacture of Protein Pharmaceuticals*, Kluwer Academic/Plenum Publishers, New York, USA **2002**, p. 281.

[11] M. C. Homola, P. J. Nicklasson, P. A. Sundsbø, *Cold Reg. Sci. Technol.* **2006**, *46*, 125.

[12] T.-S. Kim, H. Park, K. Ko, G. Lim, Y.-H. Cha, J. Han, D.-Y. Jeong, *Appl. Phys. B* **2010**, *100*, 437.

[13] "Introduction to body composition assessment using the deuterium dilution technique with analysis of saliva samples by Fourier transform infrared spectrometry," International Atomic Energy Agency, 2010, IAEA Human Health Series, ISSN 2075-3772; no. 12, STI/PUB/1450.

[14] a) D. Lynch, DTIC Document, **2005**; b) J. M. Labello, University of Tennesse, USA **2011**; c) T. M. Moeller, L. Smith, F. G. Collins, J. M. Labello, J. P. Rogers, H. S. Lowry, D. H. Crider, *Proc. SPIE* **2013**, *8841*, 88410R.

[15] S. Sastry, *Nature* **2005**, *438*, 746.

[16] S. G. Warren, *Appl. Opt.* **1984**, *23*, 1206.

[17] G. M. Hale, M. R. Querry, *Appl. Opt.* **1973**, *12*, 555.

[18] A. W. Snyder, J. Love, *Optical Waveguide Theory*, Springer Science & Business Media, USA **1983**.

[19] a) J. Martínez, A. Ródenas, T. Fernandez, J. R. V. de Aldana, R. R. Thomson, M. Aguiló, A. K. Kar, J. Solis, F. Díaz, *Opt. Lett.* **2015**, *40*, 5818; b) J. Guan, X. Liu, P. S. Salter, M. J. Booth, *Opt. Express* **2017**, *25*, 4845; c) H. Chandrahalim, S. C. Rand, X. Fan, *Sci. Rep.* **2016**, *6*, 32668.

[20] P. Clechet, N. Jaffrezic-Renault, *Adv. Mater.* **1998**, *2*, 293.

